Revision 2:

P–V–T equation of state of hydrous phase A up to 10.5 GPa

CUIPING YANG[1], TORU INOUE[1, 2*], AND TAKUMI KIKEGAWA[3]

[1] Geodynamics Research Center, Ehime University, Matsuyama, Ehime 790-8577, Japan

[2] Department of Earth and Planetary Systems Science & Hiroshima Institute of Plate Convergence Region Research (HiPeR), Hiroshima University, Higashi-Hiroshima, Hiroshima 739-8526, Japan

[3] Photon Factory, High Energy Accelerator Research Organization, Tsukuba, Ibaraki 305-0801, Japan

*Corresponding author Toru Inoue

E-mail: toinoue@hiroshima-u.ac.jp

ABSTRACT

Pressure–volume–temperature (*P–V–T*) data of synthetic $Mg_7Si_2O_8(OH)_6$ phase A, were collected under P–T conditions up to approximately 10.5 GPa and 900 K by energy dispersive X-ray diffraction using a cubic type multi-anvil apparatus, MAX80, located at the Photon Factory – Advanced Ring (PF–AR) at the High Energy Accelerator Research Organization (KEK). P-V EoS using only room temperature data yielded V_0=511.6 (2) Å^3, K_{T0}=106.8 (18) GPa, and pressure derivative K_T'=3.88 (38). These properties were consistent with the subsequent equation of state (EoS) analysis. The compressibility of phase A was very anisotropic along the axes, with the *a*-axis as approx. 26% more compressible than the *c*-axis, which is normal to the

plane of the distorted close-packed layers. A fit of the present data to the high-temperature Birch–Murnaghan EoS yielded V_0=511.7 (3) Å^3, K_0=104.4 (24) GPa, K'=4.39 (48), $(\partial K_T/\partial T)_P$= -0.027 (5) GPa K^{-1}, and thermal expansion $\alpha=a+bT$ with values of a = 2.88 (27) × 10^{-5} K^{-1} and b= 3.54 (68) × 10^{-8} K^{-2}. The lattice dynamical approach by the Mie–Grüneisen–Debye EoS yielded θ_0=928 (114) K, q =2.9 (10), and γ_0=1.19 (8). The isobaric heat capacity C_P of phase A at 1 atm. was calculated based on the Mie–Grüneisen–Debye EoS fit of present P–V–T data. In addition, the density of subducting slab with different degree of serpentinization was also calculated along the cold geotherm up to ~13GPa. The serpentinization of subducting slab will significantly lower the density of slab at shallower depth, however, this effect becomes negligible when antigorite dehydrated to phase A. Because the phase A bearing subducting slab is supposed to be denser than the surrounding mantle, the water can transport into deeper parts of the upper mantle and the mantle transition zone.

Keywords: bulk modulus, phase A, dense hydrous magnesium silicate (DHMS), equation of state (EoS), heat capacity, high pressure and high temperature (HPHT), thermal expansion

INTRODUCTION

Dense hydrous magnesium silicate minerals (DHMS) are potential water carriers in the deep mantle. Phase A is one group of these phases that lies on the forsterite–brucite interface in the MgO-SiO$_2$-H$_2$O (MSH) system with an ideal

formula of $Mg_7Si_2O_8(OH)_6$. Its water content is about 12 wt%. In a water-saturated peridotite system, serpentine decomposes to phase A, clinoenstatite and water at 6.2 GPa, 853 K (Schmidt & Poli 1998). Ohtani et al. (2004) suggested that the serpentine transformed to phase A at depth greater than 180 km (~6 GPa) in a cool subducting slab, and that phase A was stable up to 11 GPa before hydrous phase E becomes the main water carrier in the slab. Komabayashi et al. (2005a) conducted experiments to examine antigorite bulk composition and pointed out that antigorite breaks down to phase A + enstatite + water at ~5 GPa, 823 K. Komabayashi et al. (2005b) also conducted experimental and theoretical study of stability of phase A and derived the thermochemical parameters. Therefore, phase A is an important water carrier in the subduction zone after antigorite is dehydrated. Its EoS has been of particularly interest.

The EoS of Fe-free phase A was reported in several studies. A range of values for bulk moduli (K_0) and the pressure derivative (K') has also been reported. Pawley et al. (1995) investigated the thermal expansivity and compressibility of phase A in the MSH system. They reported a value of K_0 = 145 (5) GPa (K' fixed to 4), thermal expansion α_0 = 4.9 (2) × 10^{-5}/K, and obtained the temperature derivative of bulk modulus $(\partial K_T/\partial T)_P$= -0.049 GPa/K using the empirical equation $(\partial K_T/\partial T)_P$= $-7\alpha K_0$. Kuribayashi et al. (2003) found that K_0 = 105 (4) GPa and K' = 3.9 (8) from single-crystal X-ray diffraction (XRD) up to 11.2 GPa. The Kuribayashi's bulk modulus was markedly lower than the Pawley's one. Crichton and Ross (2002) also measured the lattice parameters using single crystal and obtained K_0 = 97.5(4) GPa,

68 K' = 5.97 (14). The datasets from Crichton and Ross (2002) and from Kuribayashi et
69 al. (2003) were mutually consistent when considering the tradeoff between K and K'.
70 Recently, Holl et al. (2006) studied the Fe-bearing phase A, $Mg_{6.85}Fe_{0.14}Si_2O_8(OH)_6$
71 using single-crystal XRD up to 33 GPa at room temperature. They reported the value
72 of K_0 = 102.9 (28) GPa and K' = 6.4 (3). In addition, Sanchez-Valle et al. (2006, 2008)
73 determined the single crystal elastic properties of phase A by Brillouin spectroscopy,
74 and obtained the adiabatic bulk and shear moduli and the derivatives, K_s = 106 (1)
75 GPa, K' = 5.8 (3) and μ = 61 (1) GPa and μ' = 1.8 (1). Nevertheless, few experiments
76 were done under high-temperature conditions. No report of the relevant literature
77 describes an experiment conducted under conditions of simultaneous high pressure
78 and high temperature (HPHT).

79 To investigate the thermoelastic properties (e.g., temperature dependence of bulk
80 modulus, thermal expansion, etc.) of phase A, we conducted *P–V–T* experiments
81 under conditions of simultaneous HPHT on synthetic phase A by synchrotron powder
82 XRD up to ~10.5 GPa and 900 K. Results are compared with those of earlier studies.
83 The Mie–Grüneisen–Debye EoS of phase A was also reported.

84 # EXPERIMENTAL METHODS

85 ## Synthesis of Phase A

86 Phase A was synthesized using powder mixture of MgO, $Mg(OH)_2$ and SiO_2, in
87 the Kawai-type (MA8-type) high pressure apparatus, ORANGE 1000, in the
88 Geodynamics Research Center (GRC), Ehime University, Japan. 14/8 type cell

assembly was used. That is, the edge length of the octahedron pressure medium is 14 mm. The truncation edge length (TEL) of the second stage tungsten carbide is 8 mm. Semi-sintered MgO doped with 17% CoO was used as the pressure medium. For this study, $LaCrO_3$ was used as a thermal insulator; Pt foil of 30 μm thickness was used as both a heater and a sample container. The cell was compressed to 11 GPa and heated to 1123 K for 30 minutes, and the charge was quenched by turning off the electric power supply. Then the pressure was released gradually for ~10 hours.

The recovered sample was not well sintered. It was easily crushed to powder by agate mortar to be submicron grain size. The powder XRD pattern of the recovered sample showed that it is pure phase A.

In-situ X-ray diffraction

HPHT synchrotron XRD experiments were conducted using a 6-6 type multi-anvil (6-6 type MA) assembly operated in a cubic anvil (DIA) apparatus, MAX80, at beam-line AR-NE5C at the PF-AR, Tsukuba, Japan. Details of 6-6 type MA were described by Nishiyama et al. (2008). Figure 1 shows the cell assemblage used for *in-situ* X-ray diffraction experiments, which was the same as that used by Yang et al. (2014). The powdered sample and pressure standard were placed into NaCl sleeves. Cylindrical graphite was used as a furnace, whereas ZrO_2 sleeve with h-BN X-ray window was used as a thermal insulator. Cubic-shaped boron epoxy was used as the pressure medium. The temperature was monitored with a $W_{97\%}Re_{3\%}$-$W_{75\%}Re_{25\%}$ thermocouple. The junction of thermocouple was sandwiched in the center of the

furnace between the pressure standard and the sample. Pressure effects on the electromotive force (EMF) of the thermocouple were neglected during temperature measurements. A mixture of NaCl and Au with a weight ratio of 10:1 was used as a pressure standard.

The energy dispersive X-ray diffraction method was used in the current study. The incident beam was collimated to a rectangular shape with 100 μm in vertical and 200 μm in horizontal by slits. Data were collected using a solid-state detector (SSD) connected to a multi-channel analyzer, which was calibrated with the characteristic X-rays of several metal standards: Cu, Ag, Pr, Dy, W, Er, Au, Bi, Pb, Ta, and La. The X-rays diffracted from the sample and pressure marker were collected at a fixed 2θ angle of ~6° in the vertical direction. The 2θ angle was calibrated by the unit cell volume of NaCl at ambient conditions. To minimize the pressure and temperature uncertainty, XRD data of both the sample and pressure marker were collected at positions as close as possible to the thermocouple junction.

The pressures were calculated from the EoS of NaCl proposed by Decker (1971). XRD patterns were analyzed using a program, *XRayAna*, by which the unit cell parameters were calculated from the peak positions using least-squares method. To calculate the unit cell parameters, 5–7 diffraction peaks from NaCl and 6–11 peaks from phase A were used.

In the *P–V–T* experiments, the cell was compressed to a desired load after the diffraction patterns were collected at ambient conditions. Then it was heated to a

desired temperature to anneal the sample. The first cycle was heated to 773 K. It was efficient to remove the deviatoric stress because the diffraction peaks became sharp after heating. Diffraction patterns were collected at every 100 K interval during cooling. After data collection at room temperature, the cell was compressed further to the next desired pressure. Similar cycles for data collection were repeated. Figure 2 portrays the pressure–temperature paths of the *P–V–T* experiments. As shown in Table 1, we collected 49 data points.

RESULTS AND DISCUSSION

Room temperature equation of state

The unit cell parameters of phase A obtained at ambient conditions were a=7.858 (4) Å, c=9.566 (8) Å, which were consistent with results reported from earlier studies (Horiuchi et al. 1979; Pawley et al. 1995; Kagi et al. 2000; Crichton and Ross 2002). Figure 3 presents unit cell volumes at room temperature against pressure. Those room temperature data were fitted with the Birch–Murnaghan EoS, which is

$$P = \frac{3K_{T0}}{2}\left[\left(\frac{V}{V_0}\right)^{-7/3} - \left(\frac{V}{V_0}\right)^{-5/3}\right]\left\{1 + \frac{3}{4}\left(K'_{T0} - 4\right)\left[\left(\frac{V}{V_0}\right)^{-2/3} - 1\right]\right\}, \quad (1)$$

where V_0, K_0, and K_0' respectively denote the unit cell volume, the isothermal bulk modulus, and its pressure derivative. The fitted curve is shown as the solid line in Figure 3, which yields values of V_0=511.6 (1) Å^3, K_0=106.3 (6) GPa, with K_0' fixed as 4. Comparison of the value of K_0 revealed that phase A is more compressible than forsterite (K_0= 125 (2) GPa, Downs et al. 1996) and the hydroxyl chondrodite

(K_0=115.0 (8) GPa, Ross and Crichton 2001).

In Figure 3, data reported from earlier studies (Pawley et al. 1995; Crichton and Ross 2002; Kuribayashi et al. 2003; Holl et al. 2006) are shown for comparison. Our data show good agreement with the single-crystal diffraction data reported by Crichton and Ross (2002) and by Kuribayashi et al. (2003). Although Pawley et al. (1995) gave larger volume under high pressure, which might be attributable to the non-hydrostatic pressure in their cell assembly, as reported by Crichton and Ross (2002). Holl et al. (2006) used Fe-bearing phase A. Their data show slightly greater volume and are more compressible than the Mg end-member phase A under high pressure.

The linear compressibilities of phase A along the *a*-axis and *c*-axis are very anisotropic (Fig. 4). Linear compressibility of the *c*-axis is βc=2.21(1) × 10^{-3}/GPa, and is approximately 26% less compressible than the *a*-axis (βa=2.96(3) ×10^{-3}/GPa) because the *c*-direction is normal to the closest packed oxygen array in the structure.

High-temperature Birch–Murnaghan equation of state

We used two thermal EoS to analyze the *P–V–T* data and to extract thermoelastic parameters of phase A: high-temperature Birch–Murnaghan (HTBM) EoS and Mie–Grüneisen–Debye (MGD) EoS.

The HTBM EoS is described again by *Eq*. (1), but the V_0, K_0, and K_0' are replaced respectively by parameters at atmospheric pressure and at a constant temperature *T*: V_{0T}, K_T, and K_T'. Temperature effects for K_T and V_{0T} are given as

This is the peer-reviewed, final accepted version for American Mineralogist, published by the Mineralogical Society of America.
The published version is subject to change. Cite as Authors (Year) Title. American Mineralogist, in press.
DOI: https://doi.org/10.2138/am-2020-7132. http://www.minsocam.org/

$$K_T = K_{T0} + (\partial K_T/\partial T)_P (T - T_0) \quad (2)$$

$$V_{0T} = V_0 \, exp[\int_{T_0}^{T} \alpha dT] \quad (3)$$

where $(\partial K_T/\partial T)_P$, T_0, and α respectively represent the temperature derivative of the bulk modulus, the reference temperature (300 K), and the volumetric thermal expansion at atmospheric pressure. Thermal expansion α is represented empirically (e.g. Nishihara et al. 2005) as

$$\alpha(0,T) = a + bT. \quad (4)$$

The K_T' was assumed to be constant against temperature. Six parameters must be fitted in this approach: V_0, K_{T0}, K_T', $(\partial K_T/\partial T)_P$, a, and b. Table 2 presents the thermoelastic parameters derived by fitting our *P*–V–*T* data to the HTBM EoS and MGD EoS in addition to parameters reported in earlier studies. The data points below 873 K were used for the fitting because of a few data set at 973 K (See Fig. 2). The root mean square (RMS) misfit in pressure in the EoS fitting is also shown in Table 2, which is very low (0.075 GPa) and which is similar to the uncertainty of the experimental pressure. This low misfit is related to the very good internal consistency of our *P*–V–*T* data. Figure 5 presents the isothermal compression curves calculated from the obtained thermoelastic parameters. Apparently, our data are well fitted. Thermoelastic parameters derived from this study show good agreement with results reported by Kuribayashi et al. (2003) and by Crichton and Ross (2002). The temperature derivative of the bulk modulus $(\partial K_T/\partial T)_P$ was determined for the first

192 time based on a series of direct measurements. The smaller value means that the bulk
193 modulus is less dependent on the temperature than in the result reported by Pawley et
194 al. (1995), who calculated that value empirically. The volumetric thermal expansion at
195 atmospheric pressure and room temperature is 3.9×10^{-5}/K, which is slightly lower
196 than the value reported by Pawley et al. (1995).

197 Mie–Grüneisen–Debye equation of state

198 The *P*–*V*–*T* data were also analyzed using the Mie–Grüneisen–Debye (MGD) EoS
199 (e.g., Jackson and Rigden 1996; Tange et al. 2012). The pressure can be expressed as
200 the sum of the static pressure at room temperature $P(V,T_0)$ and thermal pressure ΔP_{th}
201 at any temperature T and given volume V (e.g. Anderson 1984). Eq. (1) was used as
202 the expression of the static pressure P (V, T_0). The Debye model was used for the
203 thermal pressure part ΔP_{th} (MGD model) (e.g., Jackson and Rigden 1996; Poirier
204 2000),

205 $$\Delta P_{th}(V,T) = \frac{\gamma}{V}[E_{th}(V,T) - E_{th}(V,T_0)] \quad , \qquad (5)$$

206 where $E_{th}(V,T)$ and γ respectively represent the internal thermal energy and the
207 Grüneisen parameter. The internal thermal energy is calculable based on the Debye
208 model as

209 $$E_{th}(V,T) = 9nRT\left[\frac{\theta}{T}\right]^{-3}\int_0^{\frac{\theta}{T}}\frac{x^3}{e^x-1}dx, \qquad (6)$$

210 where n, R, and θ respectively denote the number of atoms per formula unit, the gas

211 constant, and the Debye temperature. The Grüneisen parameter γ and the volume
212 dependence of the Debye temperature are expressed below (e.g., Nishihara et al. 2005;
213 Tange et al. 2009).

214 $$\gamma(V) = \gamma_0 \left(\frac{V}{V_0}\right)^q \quad (7)$$

215 $$\theta = \theta_0 \, exp\left(\frac{\gamma_0 - \gamma}{q}\right) \quad (8)$$

216 Therein, q is a dimensionless parameter. For this approach, six parameters must be
217 fitted: V_0, K_{T0}, K'_T, θ_0, q, and γ_0.

218 Table 2 presents results of MGD EoS fit. The V_0, K_{T0}, and K'_T values are consistent
219 with the HTBM analyses within uncertainty. The thermal parameters are found as θ_0=
220 929 (114) K, q=2.9 (10), and γ_0=1.19 (8).

221 The MGD EoS includes the expression of thermal energy (*Eth*). Therefore, we were
222 able to calculate the heat capacity of phase A from the MGD EoS parameters in Table
223 2 (Jackson and Rigden 1996; Poirier 2000). The isochoric heat capacity C_V is
224 calculated by taking the partial derivative of thermal energy *Eth* with respect to
225 temperature T ($C_V = (\partial E_{th}/\partial T)_V$), then the isobaric heat capacity C_P is obtainable by
226 conversion of the isochoric heat capacity C_V using the thermodynamic relation of
227 $C_P = C_V(1+\alpha\gamma T)$. Figure 6 presents the calculated C_P of phase A at atmospheric
228 pressure. The value estimated by Holland and Powell (1998) is also shown for
229 comparison. Data obtained under lower temperatures are mutually consistent within
230 uncertainty, although our results obtained under higher temperatures have a slightly

231 higher value than those reported from an earlier study. This report is the first to
232 describe the heat capacity of phase A based on experimental data.

233

234 ## IMPLICATIONS

235 Oceanic lithosphere consists of a thin layer oceanic crust (MORB), harzburgite,
236 residual lherzolite and depleted pyrolite (Ringwood, 1982) for the schematic profile of
237 oceanic lithosphere. Considering the water saturated upper part of the oceanic
238 lithosphere, i.e, the oceanic crust and harzburgite part, the subducting slab was
239 modeled by a combination of 80% harzburgite + 20% MORB, in which, the
240 harzburgite consists of 80% olivine + 20% pyroxene. The addition of H_2O to this
241 ultramafic bulk composition may generate serpentine by serpentinization of the
242 ultramafic rocks. Antigorite is the stable serpentine mineral in ultramafic rocks
243 metamorphosed under the moderate temperatures of blue schist and green schist
244 facies conditions (Evans, 1976; Evans, 1977; Evans, 2004), and the antigorite will be
245 stable to ~200 km before dehydrated to hydrous phase A (Bromiley and Pawley, 2003;
246 Komabayashi et al., 2005a; Ulmer and Trommsdorff, 1995; Wunder and Schreyer,
247 1997). Here, we calculated the density profile of subducting slab with different degree
248 of serpentinization by using the new thermoelastic parameters of antigorite (Yang et al,
249 2014) and phase A, and discussed the effect of serpentinization on the density of
250 subducting slab.

251 Thermoelastic parameters of mineral phases used for the density calculation were

252 listed in Table 3. The density of each mineral phase was calculated along the cold
253 geotherm (Komabayashi et al., 2005b), and then the density of harzburgite was
254 modeled by 80% olivine and 20% pyroxene. Effect of degree of serpentinization on
255 the density was calculated by using the antigorite/phase A instead of olivine, e.g. ,
256 harzburgite with 10% serpentinization means 10% olivine changes to antigorite at
257 shallow depth; the antigorite dehydrates to hydrous phase A + Enstatite +water
258 (5Atg=2PhA+8En+14H_2O) at 6GPa (e.g. Ohtani et al., 2004), and we assumed that
259 the water from this reaction was escaped from the system by migrating upwards. See
260 Figure 7 (a) for the density profiles of harzburgites. The density profile of MORB
261 from Irifune and Ringwood (1987) was employed to calculate the density of
262 subducting slab. The density of subducting slab was modeled by 80% harzburgite and
263 20% MORB (Figure 7 (b)). The density of surrounding mantle was indicated by the
264 profile of AK135 (Kennett et al., 1995). The model calculation shows that the
265 serpentinization of subducted slab decreases the density significantly at shallower
266 depth, however, this effect become negligible when antigorite dehydrated to phase A
267 at ~200km depth. Because the phase A bearing subducting slab is supposed to be
268 denser than the surrounding mantle, the water can transport into deeper parts of the
269 upper mantle and the mantle transition zone.

270 ## ACKNOWLEDGMENTS

271 This work was conducted as a part of a Ph. D. thesis of C. Yang at Ehime
272 University. We acknowledge A. Yamada, N. Cai, H. Suenami, and S. Kakizawa for
273 their great help with *in-situ* experiments at KEK. The *in-situ* X-ray measurements

were conducted at PF-AR, KEK (proposal no. 2011G100 and 2013G140 by T. Inoue).

FUNDING

This study was supported by JSPS KAKENHI Grant Numbers 20244086, 26247073, 15H05828, 18H03740, and 19KK0085 to T. Inoue.

REFERENCES CITED

Anderson, O.L. (1984) A universal thermal equation-of-state. Journal of Geodynamics, 1(2), 185-214.

Bromiley, G.D., and Pawley, A.R. (2003) The stability of antigorite in the systems MgO-SiO_2-H_2O (MSH) and MgO-Al_2O_3-SiO_2-H_2O (MASH): The effects of Al^{3+} substitution on high-pressure stability. American Mineralogist, 88(1), 99-108.

Crichton, W.A., and Ross, N.L. (2002) Equation of state of dense hydrous magnesium silicate phase A, $Mg_7Si_2O_8(OH)_6$. American Mineralogist, 87(2-3), 333-338.

Decker, D.L. (1971) High-Pressure Equation of State for NaCl, KCl, and CsCl. Journal of Applied Physics, 42(8), 3239-3244.

Downs, R.T., Zha, C.-S., Duffy, T.S., and Finger, L.W. (1996) The equation of state of forsterite to 17.2 GPa and effects of pressure media. American Mineralogist, 81(1-2), 51-55.

Evans, B. (1976) Stability of chrysotile and antigorite in the serpentine multisystem. Schweiz. Mineral. Petrogr. Mitt., 56, 79-93.

Evans, B.W. (1977) Metamorphism of alpine peridotite and serpentinite. Annual Review of Earth and Planetary Sciences, 5(1), 397-447.

Evans, B.W. (2004) The serpentinite multisystem revisited: chrysotile is metastable. International Geology Review, 46(6), 479-506.

Holl, C., Smyth, J., Manghnani, M., Amulele, G., Sekar, M., Frost, D., Prakapenka, V., and Shen, G. (2006) Crystal structure and compression of an iron-bearing phase A to 33 GPa. Physics and Chemistry of Minerals, 33(3), 192-199.

Holland, T.J.B., and Powell, R. (1998) An internally consistent thermodynamic

dataset for phases of petrological interest. Journal of Metamorphic Geology, 16(3), 309-343.

Holland, T.J.B., Redfern, S.A.T., and Pawley, A.R. (1996) Volume behavior of hydrous minerals at high pressure and temperature. 2. Compressibilities of lawsonite, zoisite, clinozoisite, and epidote. American Mineralogist, 81(3-4), 341-348.

Horiuchi, H., Morimoto, N., Yamamoto, K., and Akimoto, S. (1979) Crystal structure of $2Mg_2SiO_4 \cdot 3Mg(OH)_2$, a new high-pressure structure type. American Mineralogist, 64, 593-598.

Irifune, T., and Ringwood, A.E. (1987) Phase transformations in a harzburgite composition to 26 GPa: implications for dynamical behaviour of the subducting slab. Earth and Planetary Science Letters, 86(2-4), 365-376.

Jackson, I., and Rigden, S.M. (1996) Analysis of P–V–T data: constraints on the thermoelastic properties of high-pressure minerals. Physics of the Earth and Planetary Interiors, 96(2-3), 85-112.

Kagi, H., Parise, J.B., Cho, H., Rossman, G.R., and Loveday, J.S. (2000) Hydrogen bonding interactions in phase A [$Mg_7Si_2O_8(OH)_6$] at ambient and high pressure. Physics and Chemistry of Minerals, 27(4), 225-233.

Kennett, B.L.N., Engdahl, E.R., and Buland, R. (1995) Constraints on seismic velocities in the Earth from traveltimes. Geophysical Journal International, 122(1), 108-124.

Komabayashi, T., Hirose, K., Funakoshi, K., and Takafuji, N. (2005a) Stability of phase A in antigorite (serpentine) composition determined by *in-situ* X-ray pressure observations. Physics of the Earth and Planetary Interiors, 151(3-4), 276-289.

Komabayashi, T., Omori, S., and Maruyama, S. (2005b) Experimental and theoretical study of stability of dense hydrous magnesium silicates in the deep upper mantle. Physics of the Earth and Planetary Interiors, 153(4), 191-209.

Kuribayashi, T., Kudoh, Y., and Kagi, H. (2003) Compressibility of phase A, $Mg_7Si_2H_6O_{14}$ up to 11.2 GPa. Journal of Mineralogical and Petrological Sciences,

98(6), 215-234.

Liu, W., and Li, B. (2006) Thermal equation of state of $(Mg_{0.9}Fe_{0.1})_2SiO_4$ olivine. Physics of The Earth and Planetary Interiors, 157(3-4), 188-195.

Nishihara, Y., Nakayama, K., Takahashi, E., Iguchi, T., and Funakoshi, K. (2005) P–V–T equation of state of stishovite to the mantle transition zone conditions. Physics and Chemistry of Minerals, 31(10), 660-670.

Nishiyama, N., Wang, Y., Sanehira, T., Irifune, T., and Rivers, M., (2008) Development of the Multi-anvil Assembly 6-6 for DIA and D-DIA type high-pressure apparatuses. High Pressure Research, 28, 307-314.

Ohtani, E., Litasov, K., Hosoya, T., Kubo, T., and Kondo, T. (2004) Water transport into the deep mantle and formation of a hydrous transition zone. Physics of the Earth and Planetary Interiors, 143-144, 255-269.

Pawley, A.R., Redfern, S.A.T., and Wood, B.J. (1995) Thermal expansivities and compressibilities of hydrous phases in the system MgO-SiO_2-H_2O: talc, phase A and 10 Å phase. Contribution of Mineralogy and Petrology, 122(3), 301-307.

Poirier, J.-P. (2000) Introduction to the Physics of the Earth's Interior. Institut de France, Paris

Ringwood, A.E. (1982) Phase transformations and differentiation in subducted lithosphere: Implications for mantle dynamics, basalt petrogenesis, and crustal evolution. The Journal of Geology, 90(6), 611-643.

Ross, N.L., and Crichton, W.A. (2001) Compression of synthetic hydroxylclinohumite $[Mg_9Si_4O_{16}(OH)_2]$ and hydroxylchondrodite $[Mg_5Si_2O_8(OH)_2]$. American Mineralogist, 86(9), 990-996

Sanchez-Valle, C., Sinogeikin, S.V., Smyth, J.R., and Bass, J.D. (2006) Single-crystal elastic properties of dense hydrous magnesium silicate phase A. American Mineralogist, 91 (5-6), 961–964.

Sanchez-Valle, C., Sinogeikin, S.V., Smyth, J.R., and Bass, J.D. (2008) Sound velocities and elasticity of DHMS phase A to high pressure and implications for seismic velocities and anisotropy in subducted slabs. Physics of the Earth and Planetary Interiors, 170 (3-4), 229–239.

Schmidt, M.W., and Poli, S. (1998) Experimentally based water budgets for dehydrating slabs and consequences for arc magma generation. Earth and Planetary Science Letters, 163 (1-4), 361-379.

Tange, Y., Kuwayama, Y., Irifune, T., Funakoshi, K., and Ohishi, Y. (2012) P–V–T equation of state of $MgSiO_3$ perovskite based on the MgO pressure scale: A comprehensive reference for mineralogy of the lower mantle. Journal of Geophysical Research, 117(B6), B06201.

Tange, Y., Nishihara, Y., and Tsuchiya, T. (2009) Unified analyses for P–V–T equation of state of MgO: A solution for pressure-scale problems in high P-T experiments. Journal of Geophysical Research, 114(B3), B03208.

Ulmer, P., and Trommsdorff, V. (1995) Serpentine stability to mantle depths and subduction-related magmatism. Science, 268(5212), 858-861.

Wunder, B., and Schreyer, W. (1997) Antigorite: High-pressure stability in the system MgO-SiO_2-H_2O (MSH). Lithos, 41(1-3), 213-227.

Yang, C., Inoue, T., Yamada, A., Kigekawa, T., and Ando, J. (2014) Equation of state and phase transition of antigorite under high pressure and high temperature. Physics of the Earth and Planetary Interiors, 228, 56-62.

Zhao, Y., Schiferl, D., and Shankland, T. (1995) A high P-T single-crystal X-ray diffraction study of thermoelasticity of $MgSiO_3$ orthoenstatite. Physics and Chemistry of Minerals, 22(6), 393-398.

382 **TABLE 1.** Lattice parameters and the unit-cell volume of phase A at each P-T
383 condition

No.	Pressure (GPa)	T (K)	a (Å)	c (Å)	V (Å^3)
AR198001	0.01 (1)	300	7.858 (4)	9.566 (8)	511.6 (7)
AR198010	6.12 (6)	300	7.713 (2)	9.433 (5)	485.9 (4)
AR198018	7.10 (8)	300	7.690 (2)	9.416 (5)	482.3 (3)
AR198031	8.07 (8)	300	7.670 (1)	9.393 (2)	478.6 (1)
AR198040	9.56 (3)	300	7.642 (1)	9.366 (2)	473.7 (1)
AR198049	9.14 (6)	300	7.650 (1)	9.374 (2)	475.1 (1)
AR198055	7.08 (7)	300	7.690 (1)	9.415 (3)	482.1 (2)
AR198056	5.31 (6)	300	7.726 (1)	9.453 (3)	488.7 (3)
AR198009	6.17 (4)	373	7.717 (2)	9.436 (5)	486.7 (4)
AR198017	7.12 (6)	373	7.695 (2)	9.420 (5)	483.1 (4)
AR198020	8.31 (3)	373	7.669 (2)	9.393 (4)	478.5 (3)
AR198030	8.09 (5)	373	7.675 (1)	9.397 (2)	479.4 (1)
AR198039	9.62 (3)	373	7.646 (1)	9.369 (2)	474.3 (1)
AR198048	9.27 (6)	373	7.652 (1)	9.376 (2)	475.5 (1)
AR198054	7.21 (7)	373	7.693 (1)	9.419 (3)	482.7 (2)
AR198008	6.12 (7)	473	7.725 (2)	9.446 (6)	488.2 (4)
AR198016	7.16 (6)	473	7.702 (2)	9.425 (5)	484.1 (3)
AR198021	8.44 (4)	473	7.674 (2)	9.398 (4)	479.3 (3)
AR198029	8.14 (4)	473	7.680 (1)	9.404 (2)	480.4 (2)
AR198038	9.70 (3)	473	7.652 (1)	9.374 (2)	475.3 (1)
AR198047	9.45 (6)	473	7.657 (1)	9.381 (2)	476.3 (1)
AR198053	7.39 (7)	473	7.697 (1)	9.423 (2)	483.5 (2)
AR198003	6.51 (1)	573	7.728 (3)	9.447 (7)	488.7 (6)
AR198007	6.19 (5)	573	7.732 (2)	9.453 (5)	489.5 (4)
AR198015	7.24 (6)	573	7.708 (2)	9.432 (5)	485.3 (4)
AR198022	8.48 (3)	573	7.681 (2)	9.406 (4)	480.5 (3)
AR198028	8.23 (4)	573	7.687 (1)	9.410 (2)	481.5 (2)
AR198037	9.82 (2)	573	7.658 (1)	9.380 (3)	476.4 (2)
AR198046	9.63 (6)	573	7.661 (1)	9.384 (2)	477.0 (1)
AR198052	7.61 (7)	573	7.702 (1)	9.428 (2)	484.3 (2)
AR198006	6.34 (3)	673	7.741 (2)	9.462 (5)	491.0 (4)
AR198014	7.41 (9)	673	7.716 (2)	9.439 (5)	486.7 (4)
AR198023	8.53 (4)	673	7.689 (2)	9.415 (5)	482.1 (4)

This is the peer-reviewed, final accepted version for American Mineralogist, published by the Mineralogical Society of America.
The published version is subject to change. Cite as Authors (Year) Title. American Mineralogist, in press.
DOI: https://doi.org/10.2138/am-2020-7132. http://www.minsocam.org/

AR198027	8.37 (3)	673	7.694 (1)	9.418 (2)	482.8 (2)
AR198036	9.96 (2)	673	7.664 (1)	9.385 (3)	477.4 (2)
AR198045	9.86 (5)	673	7.666 (1)	9.390 (2)	477.9 (1)
AR198051	7.80 (7)	673	7.708 (1)	9.434 (2)	485.4 (2)
AR198005	6.44 (2)	773	7.748 (2)	9.472 (5)	492.4 (4)
AR198013	7.53 (7)	773	7.723 (2)	9.447 (5)	487.9 (4)
AR198024	8.61 (4)	773	7.697 (3)	9.424 (6)	483.5 (4)
AR198026	8.63 (4)	773	7.695 (3)	9.427 (6)	483.5 (5)
AR198035	10.12 (2)	773	7.669 (1)	9.391 (3)	478.3 (2)
AR198044	10.07 (6)	773	7.671 (1)	9.394 (2)	478.7 (1)
AR198012	7.61 (2)	873	7.733 (2)	9.457 (5)	489.7 (4)
AR198025	8.71 (4)	873	7.703 (3)	9.436 (7)	484.9 (5)
AR198034	10.22 (2)	873	7.675 (1)	9.397 (3)	479.3 (2)
AR198043	10.25 (7)	873	7.676 (1)	9.399 (2)	479.7 (1)
AR198033	10.32 (6)	973	7.681 (1)	9.405 (3)	480.5 (2)
AR198042	10.47 (7)	973	7.683 (1)	9.402 (3)	480.6 (3)

Parenthesis shows one standard deviation.

TABLE 2. Thermoelastic parameters of phase A from this study and earlier studies

	RT BM EoS	HT BM EoS	MGD EoS	K03	C&R02	P95	H06 #	S-V06 # $
V_0 (Å^3)	511.6 (2)	511.7 (3)	511.7 (3)	512.2 (6)	512.56 (3)	510.8	512.3 (3)	513.67
K_{T0} (GPa)	106.8 (18)	104.4 (24)	104.9 (23)	105 (4)	97.5 (4)	145 (5)	102.9 (28)	106 (1)
K_T'	3.88 (38)	4.39 (48)	4.29 (45)	3.9 (8)	5.97 (14)	4 (fixed)	6.4 (3)	5.8 (3)
dK_T/dT (GPa/K)	-	-0.027 (5)	-	-	-	-0.049*	-	-
α=a+bT	-	-	-	-	-	-	-	-
a (10^{-5}/K)	-	2.88 (27)	-	-	-	4.9 (2)	-	-
b (10^{-8}/K^2)	-	3.54 (68)	-	-	-	-	-	-
θ_0 (K)	-	-	928 (114)	-	-	-	-	-
γ_0	-	-	1.19 (8)	-	-	-	-	-
q	-	-	2.9 (10)	-	-	-	-	-
RMS misfit (GPa)		0.075	0.152					

K03:Kuribayashi et al. (2003), C&R02: Crichton and Ross (2002), P95: Pawley et al. (1995), H06: Holl et al. (2006), and S-V06: Sanchez-Valle et al. (2006). #: Fe-bearing phase A, $: adiabatic property by Brillouin spectroscopy, * calculated using empirical equation dK/dT=-7αK_{T0} (Holland et al., 1996)

This is the peer-reviewed, final accepted version for American Mineralogist, published by the Mineralogical Society of America.
The published version is subject to change. Cite as Authors (Year) Title. American Mineralogist, in press.
DOI: https://doi.org/10.2138/am-2020-7132. http://www.minsocam.org/

392 **TABLE 3.** Thermoelastic parameters used in the density calculation

Mineral	V_0 (Å^3)	K_0 (GPa)	K_0'	$(dK/dT)_P$ (GPa/K)	$a \times 10^{-5}$ (K^{-1})	$b \times 10^{-8}$ (K^{-2})	Ref.
olivine	292.13 (10)	129	4.61	-0.019 (2)	2.73 (34)	2.22 (81)	Liu and Li (2006)
enstatite	832.68 (9)	102.8 (2)	10.2 (12)	-0.037 (5)	2.86 (29)	0.72 (16)	Zhao et al. (1995)
antigorite	367.3 (2)	62.9	6.1	-0.027 (4)	3.92 (49)	-	Yang et al. (2014)
phase A	511.7 (3)	104.4 (24)	4.39 (48)	-0.027 (5)	2.88 (27)	3.54 (68)	This study

393 Parenthesis shows one standard deviation.

394

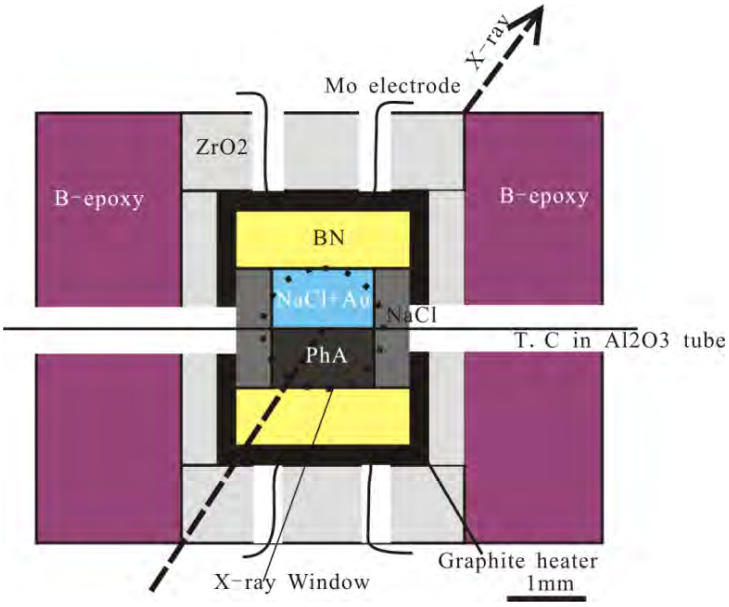

395

396 **FIGURE 1.** Cell assembly used for the present *in-situ* X-ray diffraction experiments.
397 The X-ray path is shown by the arrow and the dotted circle, representing the "X-ray
398 window" covered by h-BN in the ZrO_2 sleeve.

399

This is the peer-reviewed, final accepted version for American Mineralogist, published by the Mineralogical Society of America.
The published version is subject to change. Cite as Authors (Year) Title. American Mineralogist, in press.
DOI: https://doi.org/10.2138/am-2020-7132. http://www.minsocam.org/

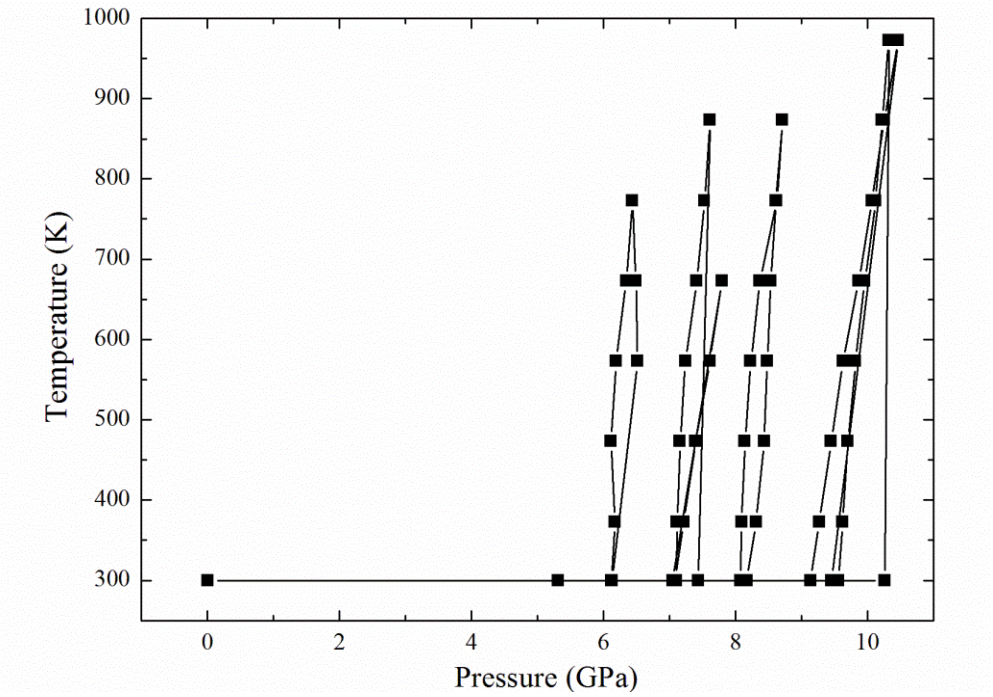

FIGURE 2. Pressure–temperature pathway of the present experiment. Most P–V–T data used for EoS analysis were collected during cooling.

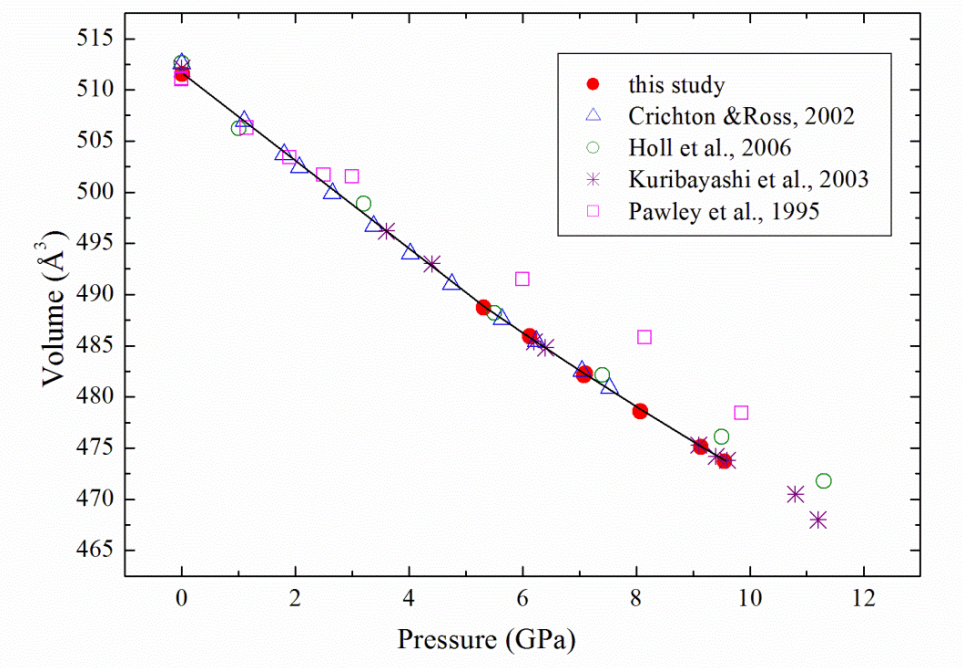

FIGURE 3. Room temperature compression data of phase A. The solid curve is the fit of room temperature data using the Birch–Murnaghan EoS. Data from earlier studies are also shown for comparison. Error bars are comparable with data markers. Data from Holl et al. (2006) are Fe-bearing phase A, whereas the others are of pure Mg end members.

This is the peer-reviewed, final accepted version for American Mineralogist, published by the Mineralogical Society of America.
The published version is subject to change. Cite as Authors (Year) Title. American Mineralogist, in press.
DOI: https://doi.org/10.2138/am-2020-7132. http://www.minsocam.org/

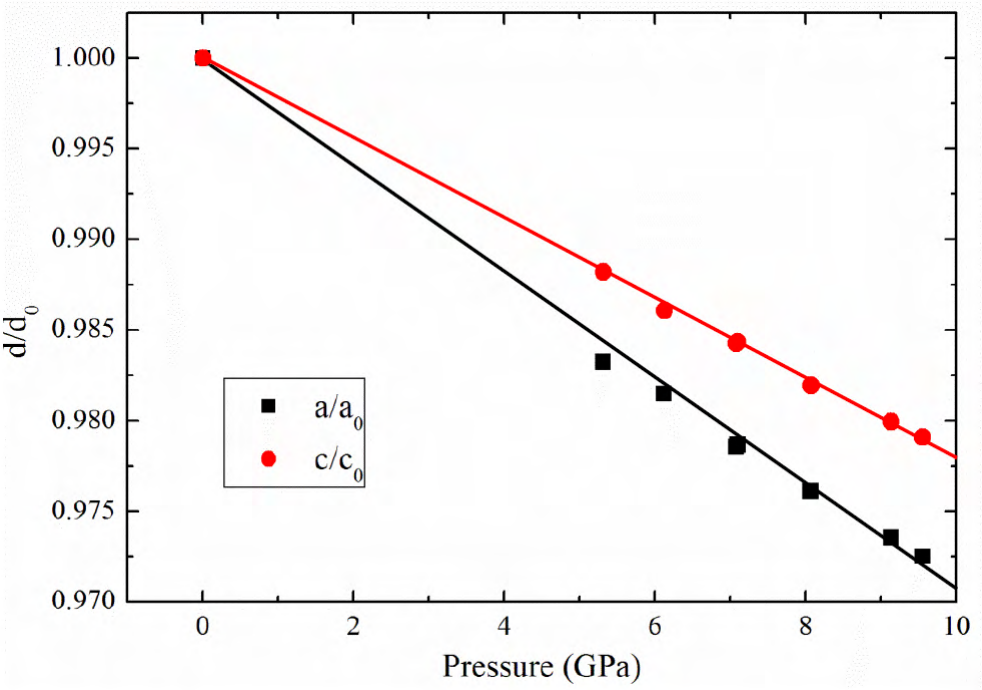

FIGURE 4. Variation of unit-cell axis length with increasing pressure at room temperature. Linear compression (β) of the a-axis and c-axis are, respectively, $\beta a=2.96(3) \times 10^{-3}$/GPa and $\beta c=2.21(1) \times 10^{-3}$/GPa. The a-axis is approximately 26% more compressible than the c-axis. Error bars are within the data markers.

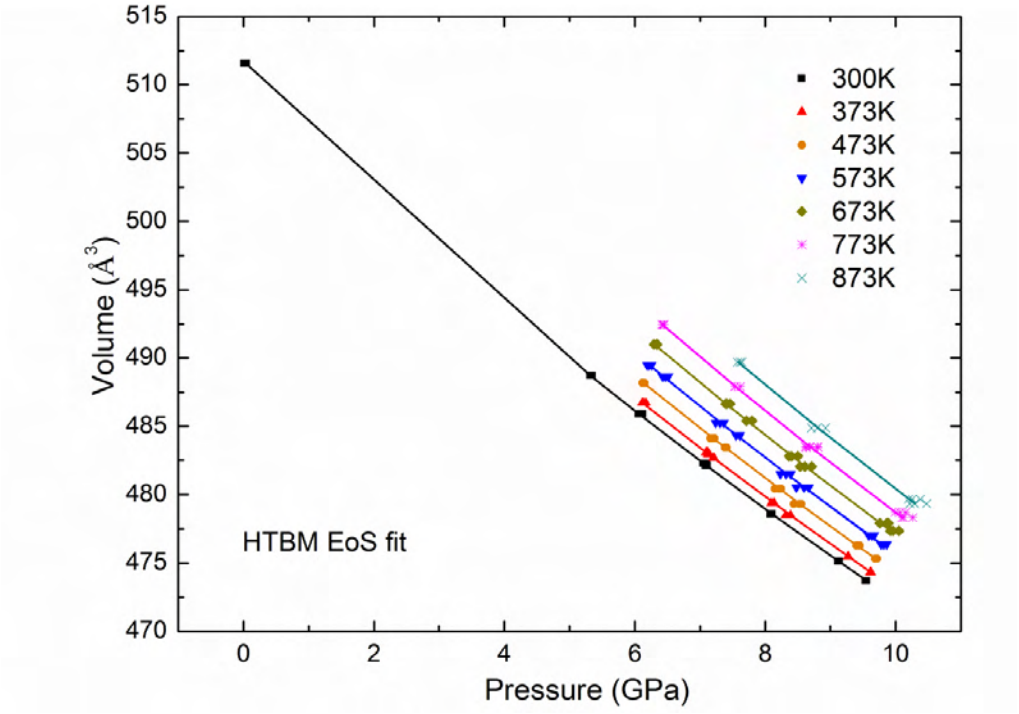

FIGURE 5. P–V–T data of phase A with the HTBM EoS fit. Solid lines are isothermal compression curves at 300 K, 373 K, 473 K, 573 K, 673 K, 773 K, and 873 K. Error bars are within the data markers.

This is the peer-reviewed, final accepted version for American Mineralogist, published by the Mineralogical Society of America.
The published version is subject to change. Cite as Authors (Year) Title. American Mineralogist, in press.
DOI: https://doi.org/10.2138/am-2020-7132. http://www.minsocam.org/

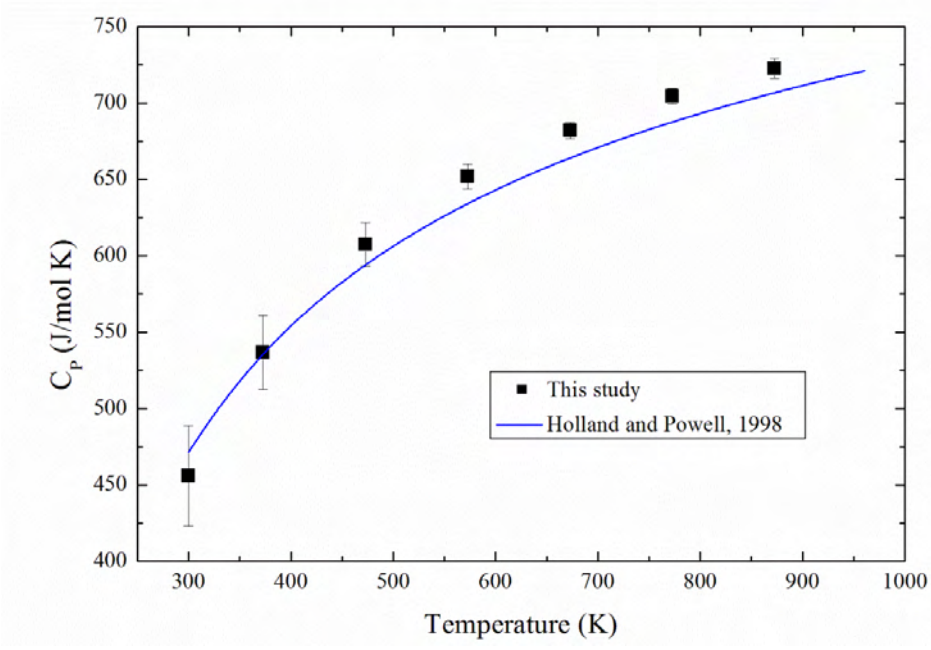

FIGURE 6. Isobaric heat capacity C_P of phase A at 1 atm. Solid squares are based on MGD EoS fit of present P–V–T data. Their error bars correspond to the error of Debye temperature θ. Values of C_P estimated by Holland and Powell (1998) are shown for comparison.

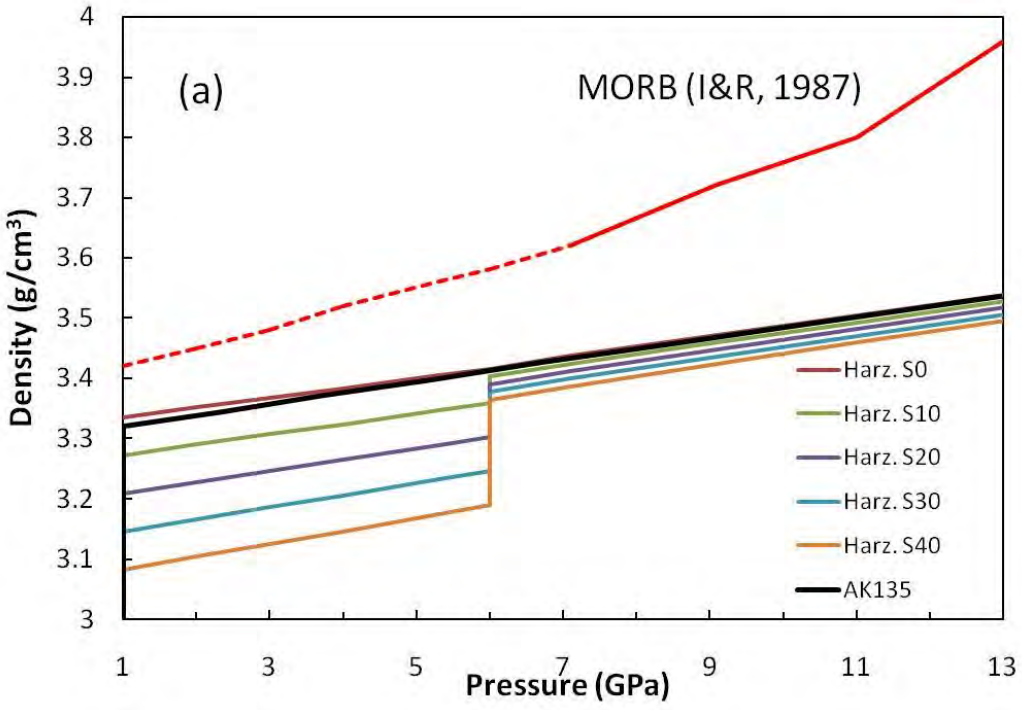

This is the peer-reviewed, final accepted version for American Mineralogist, published by the Mineralogical Society of America.
The published version is subject to change. Cite as Authors (Year) Title. American Mineralogist, in press.
DOI: https://doi.org/10.2138/am-2020-7132. http://www.minsocam.org/

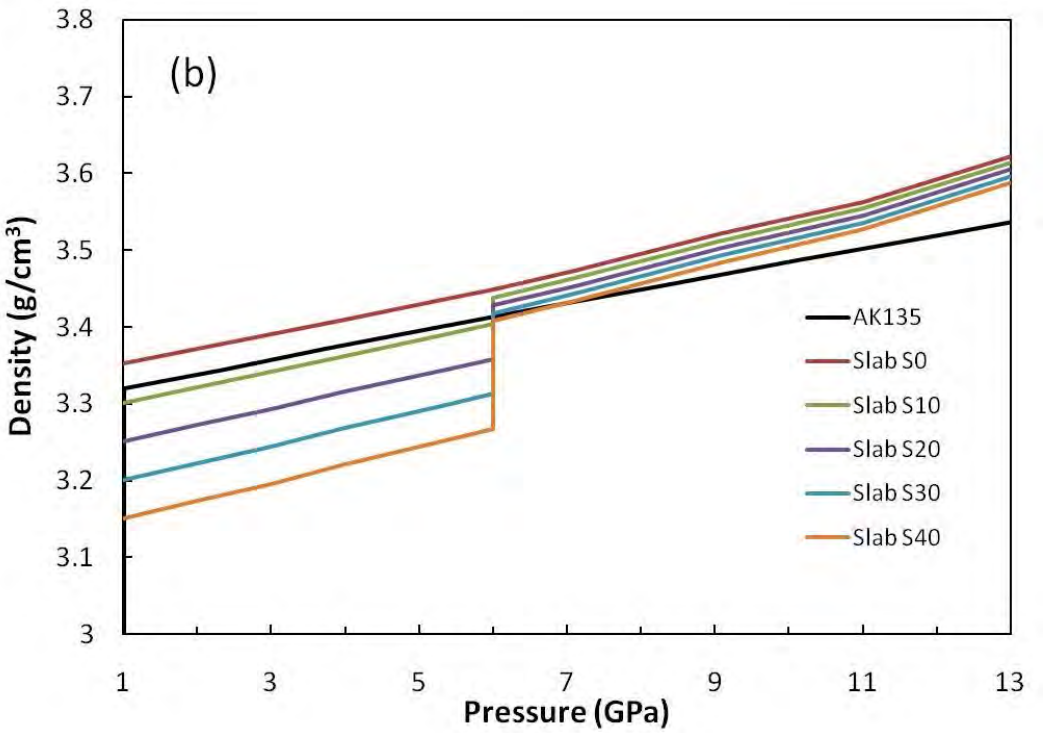

FIGURE 7. (a) Density of harzburgite and (b) subducting slab with different degree of serpentinization (S0, S10, S20, S30, S40 and S50 show the serpentinization of 0, 10, 20, 30, 40 and 50%, respectively), along cold subduction zone geotherm (Komabayashi et al., 2005b). Red line in (a) indicates the density of MORB (Irifune and Ringwood, 1987). The density of MORB at lower pressure rage (the dashed line) was estimated from the density at high pressure range. The density profile of AK135 (Kennett et al., 1995) is shown for comparison.